UNCLASSIFIED: Distribution Statement A. Approved for public release.#24028

2013 NDIA GROUND VEHICLE SYSTEMS ENGINEERING AND TECHNOLOGY SYMPOSIUM
MODELING & SIMULATION, TESTING AND VALIDATION (MSTV) MINI-SYMPOSIUM
AUGUST 21-22, 2013 - TROY, MICHIGAN

Scalability of Classical Terramechanics Models for Lightweight Vehicle Applications

Paramsothy Jayakumar
Daniel Melanz
Jamie MacLennan
U.S. Army TARDEC
Warren, MI, USA

Carmine Senatore
Karl Iagnemma
Massachusetts Institute of Technology
Cambridge, MA, USA

ABSTRACT

This paper investigates the validity of commonly used terramechanics models for light-weight vehicle applications while accounting for experimental variability. This is accomplished by means of cascading uncertainty up to the terminal point of operations measurement. Vehicle-terrain interaction is extremely complex, and thus models and simulation methods for vehicle mobility prediction are largely based on empirical test data. Analytical methods are compared to experimental measurements of key operational parameters such as drawbar force, torque, and sinkage. Models of these operational parameters ultimately depend on a small set of empirically determined soil parameters, each with an inherent uncertainty due to test variability. The soil parameters associated with normal loads are determined by fitting the dimensionless form of Bekker's equation to the data given by the pressure-sinkage test. In a similar approach, the soil parameters associated with shear loads are determined by fitting Janosi and Hanamoto's equation to the data given by the direct shear test. An uncertainty model is used to propagate the soil parameter variability through to the wheel performance based on Wong and Reece. The commonly used analytical model is shown to be inaccurate as the envelope of model uncertainty does not lie within the experimental measures, suggesting that model improvements are required to accurately predict the performance of light-weight vehicles on deformable terrain.

BACKGROUND

The study of the interaction of wheeled and tracked vehicles with natural terrain is dominated by the discipline of terramechanics. Terramechanics research over the past 50 years has primarily focused on large, heavy military vehicles. A substantial body of terramechanics research has been performed at the U.S. Army Tank Automotive Research, Development, and Engineering Center (TARDEC) and the U.S. Army Engineer Research and Development Center (ERDC) that led to the development of various mobility prediction methodologies including the NATO Reference Mobility Model (NRMM). These methodologies are numerical algorithms for predicting cross-country vehicle movement at length scales of several meters to several kilometers. They are based on empirical results drawn from years of resource-intensive experimental testing and have been used widely by the military community. However, as a consequence of their empirical nature, while the methods are useful for prediction of large, heavy vehicle mobility, it remains an open question whether they can be reliably used for the prediction of small, lightweight vehicle mobility.

Recently the Department of Defense (DoD) has devoted substantial resources toward the development of small, lightweight ground vehicles. These vehicles are often less than 36 inches in length and weigh less than 100 lb. They are equipped with wheels, tracks, or bio-inspired limb-like appendages. Due to the lack of mobility models for these vehicles, there is a lack of simulation methods for this class of vehicles. Also, since these vehicles have only recently been adopted by the DoD, there is a lack of systematic empirical test data. As a result, these vehicles have primarily been developed based on ad hoc design rules, limited empirical testing, and application of classical Bekker theory. Thus, there is a lack of methods (based on simulation or analysis) to reliably predict the mobility and performance of these systems.

This paper will describe two experimental methods used to characterize mechanical soil behavior for lightweight vehicles. A pressure-sinkage test and a standard direct shear test as outlined by Bekker in [1] were performed on a cohesion-less soil [2]. This paper investigates identification of soil parameters from the experimental data and assesses the data variability, which is inherent in both tests. The variability in the soil parameters is propagated to determine the overall wheel performance

uncertainty. Probabilistic, rather than strictly deterministic, soil behavior is considered in this paper because it is an increasingly important consideration for accurate modeling of lightweight robotic vehicle performance.

METHODOLOGY

Semi-empirical methods for modeling wheel performance, like the one used in this paper by Wong and Reece [3], rely on the relationship between soil sinkage and resistance force to infer the normal stress under a wheel. To predict the tractive force, the shearing strength of the soil is analyzed based on Coulomb's formula [4]. Methods of this class are ultimately based on experimentally determined soil parameters, whose inherent variability causes uncertainty in the determination of wheel performance. The order of the paper is as follows. The first section describes the equipment and methods used to determine the variability in soil parameters; the second section describes the wheel model in which these parameters are used and the techniques used to compare prediction to experimental data.

Soil Parameter Variability

Mojave Martian Simulant (MMS) [2] was employed as a test medium for the experiments in this paper. MMS is a mixture of finely crushed and sorted granular basalt intended to mimic, both at a chemical and mechanical level, Mars soil characteristics. No direct application to Mars rovers is provided in this paper, the simulant is a frictional soil found in dry, sandy terrain. The particle size distribution of MMS spans from the micron to millimeter level with 80% of particles above the 10 micron threshold.

Experimental Equipment

Pressure-Sinkage Test

The sinkage characteristics of the MMS were measured using the pressure-sinkage test shown in Figure 1. The pressure-sinkage test used a plate to penetrate the soil under controlled test conditions, while pressure and sinkage of the plate were directly measured. A series of tests and various plate sizes allowed an investigation of both the influence of the pressure-sinkage parameters as described in Wong's methodology [5] and test-to-test variability.

The test unit was designed to systematically penetrate the soil with a downward velocity of 10 mm/s. Penetration tests were performed with three different-sized rectangular plates (3x15, 5x15, and 7x15 cm^2). The tests were repeated 15 times for each plate. A load cell and draw-wire encoder recorded the force and corresponding sinkage during each test. Between tests, the soil was loosened with a stick and then leveled to return the MMS to a nominal density of 1.7 g/cm^3. Figure 2 shows a picture of a penetration plate about to enter the soil.

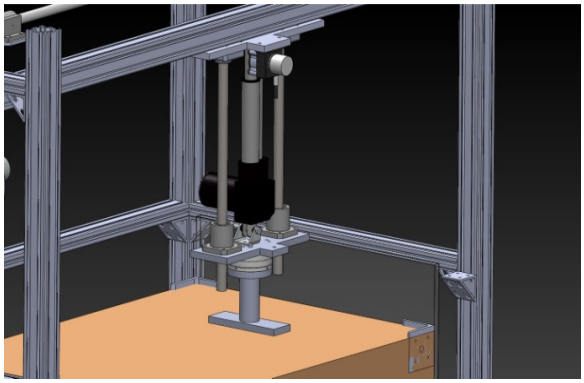

Figure 1: CAD drawing of the pressure-sinkage test rig. A load cell and draw wire encoder recorded the force and sinkage of a plate that was pressed into the soil at 10 mm/s.

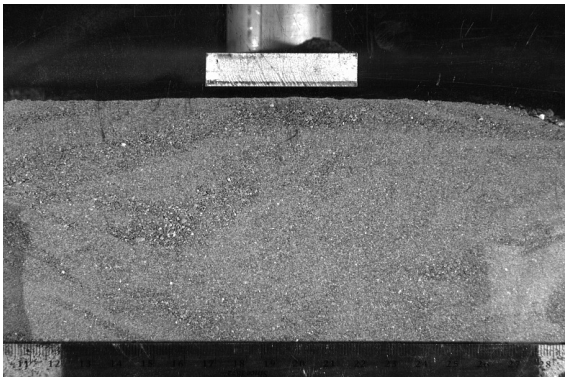

Figure 2: Penetration plate and soil (side view).

Direct Shear Test

The direct shear test, shown in Figure 3, is used to measure the shear strength properties of the MMS, specifically the cohesion, angle of friction, and shear modulus. A sample of the soil is contained in between two rigid discs that are held in place by a shear box. The shear box is aligned under a load cell that applies a normal force to the soil.

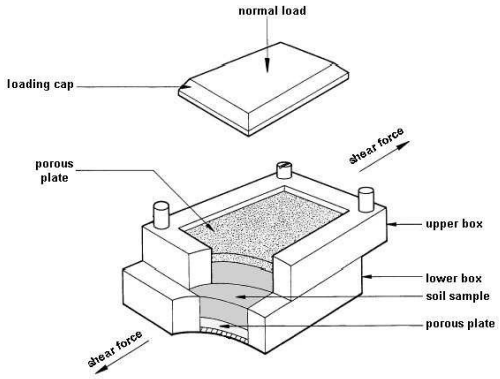

Figure 3: Experimental device for performing the direct shear test.

The load cell is attached to a vertical translational joint that uses a linear variable differential transformer to measure displacement of the soil. The top of the shear box is clamped so that the lower half can be moved. The horizontal force required to displace the soil horizontally is measured by a dynamometer. The applied vertical force and measured horizontal force can be transformed into the normal and shear stress, respectively. The horizontal and vertical soil displacement is also output.

Parameter Estimation

Pressure-Sinkage Parameter Estimation

To describe the pressure-sinkage relationship of a soil's deformation under a rectangular plate, Bekker suggested Equation (1) based on the soil mechanics work originally performed by Terzaghi [6]:

$$\sigma = \left(\frac{k_c}{b} + k_\varphi \right) z^n, \tag{1}$$

where σ is pressure, b is plate width, z is soil sinkage, and n, k_c and k_φ, are soil parameters. The three parameters are empirical and have no intrinsic physical meaning. The parameters may be estimated from experimental pressure-sinkage data if at least two different plate sizes are tested.

The process of determining the soil parameters from experimental data was originally performed by Wong using a weighted least squares method [7], which is the primary estimation technique used in this paper. From Equation (1), taking the logarithms of both sides gives:

$$\ln \sigma = \ln \left(\frac{k_c}{b} + k_\varphi \right) + n \ln z. \tag{2}$$

An error function is defined as:

$$F = w_r \left(\ln \sigma - \ln \left(\frac{k_c}{b} + k_\varphi \right) - n \ln z \right)^2, \tag{3}$$

where w_r is a weighting factor. Standard least squares minimization of equation (3) would set w_r equal to 1. However, as Wong explains, error would be biased toward low pressures since the actual measured values are σ and z, not $\ln \sigma$ and $\ln z$. To account for minimization in the log-log domain and give equal weight to all data points, Wong sets the weighting factor $w_r = \sigma^2$.

Since k_c, b, and k_φ are constant values for a given test, they can be replaced by a single constant:

$$k_{eq} = \frac{k_c}{b} + k_\varphi. \tag{4}$$

Wong provides the following cost function over N data points that is minimized to find optimal n and k_{eq} in Equation (5):

$$F = \sum_{i=1}^{N} \sigma_i^2 \left[\ln \sigma_i - \ln \left(k_{eq} \right) - n \ln z_i \right]^2. \tag{5}$$

The first order KKT optimality condition leads to the following two equations:

$$\frac{\partial F}{\partial n} = -2 \left[\sum \sigma^2 \ln \sigma \ln z - \ln k_{eq} \sum \sigma^2 \ln z - n \sum \sigma^2 \left(\ln z \right)^2 \right] = 0 \tag{6}$$

$$\frac{\partial F}{\partial k_{eq}} = \frac{-2}{k_{eq}} \left[\sum \sigma^2 \ln \sigma + 2 \ln k_{eq} \sum \sigma^2 + 2n \sum \sigma^2 \ln z \right] = 0. \tag{7}$$

Solving equations (6) and (7) for n and k_{eq}, yields:

$$n = \frac{\sum \sigma^2 \sum \sigma^2 \ln \sigma \ln z - \sum \sigma^2 \ln \sigma \sum \sigma^2 \ln z}{\sum \sigma^2 \sum \sigma^2 \left(\ln z \right)^2 - \left(\sum \sigma^2 \ln z \right)^2} \tag{8}$$

$$k_{eq} = exp\left(\frac{\sum \sigma^2 \ln \sigma - n \sum \sigma^2 \ln z}{\sum \sigma^2} \right). \quad (9)$$

If the above analysis is performed for two sets of data corresponding to two different plate sizes (b_1 , b_2), the average n and two corresponding values of k_{eq} can be found:

$$n_{av} = \frac{(n)_{b=b1} + (n)_{b=b2}}{2} \quad (10)$$

$$\left(k_{eq}\right)_{b=b_1} = \left[exp\left(\frac{\sum \sigma^2 \ln \sigma - n_{av} \sum \sigma^2 \ln z}{\sum \sigma^2} \right) \right]_{b=b_1} \quad (11)$$

$$\left(k_{eq}\right)_{b=b_2} = \left[exp\left(\frac{\sum \sigma^2 \ln \sigma - n_{av} \sum \sigma^2 \ln z}{\sum \sigma^2} \right) \right]_{b=b_2}. \quad (12)$$

Using the two values of k_{eq} , k_c and k_φ can be derived:

$$k_c = \frac{b_1 b_2}{b_2 - b_1} \left(\left(k_{eq}\right)_{b=b1} - \left(k_{eq}\right)_{b=b2} \right) \quad (13)$$

$$k_\varphi = \left(k_{eq}\right)_{b=b1} - \frac{b_2}{b_2 - b_1} \left(\left(k_{eq}\right)_{b=b1} - \left(k_{eq}\right)_{b=b2} \right). \quad (14)$$

Wong's methodology is a clear and succinct way to obtain the three pressure-sinkage soil parameters (n , k_c , k_φ) from a set of experimental data.

To avoid difficulties resulting from covariance between soil parameters, Reece's revision of Bekker's equation [3] was implemented by the authors of this paper. Reece's equation is:

$$\sigma = \left(k_1 + b k_2\right) \left(\frac{z}{b} \right)^n. \quad (15)$$

where k_1 and k_2 are empirical soil parameters. In simplified terms, Equation (15) reduces to:

$$\sigma = k_{eq}^{'} \left(\frac{z}{b} \right)^n. \quad (16)$$

where the k coefficient is denoted as $k_{eq}^{'}$ to distinguish from the k_{eq} of Bekker's equation. To provide a more thorough analysis of pressure-sinkage parameter estimation methods, four additional, modified approaches were also considered. The resulting parameters of all five methods are compared. Because Wong's pressure-sinkage relation and Reece's modification have the same format for any single plate, the results of the following methods apply equally to both.

Method 1 is performed using Wong's equations (8)-(14) previously given for individual experimental tests.

Method 2 is a modified version of the technique presented by Wong. The weighting factor w_r in equation (3) is changed from σ^2 to 1. The resulting equations for n and k_{eq} are derived analytically using a similar approach as Wong:

$$n = \frac{\sum \ln \sigma \ln z - \frac{\sum \ln \sigma \sum \ln z}{N}}{\sum \left(\ln z\right)^2 - \frac{\left(\sum \ln z\right)^2}{N}}, \quad (17)$$

$$k_{eq} = exp\left(\frac{\sum \ln \sigma - n \sum \ln z}{N} \right). \quad (18)$$

From Equation (17), k_c and k_ϕ can be derived in the same manner as equations (13) and (14).

For the final three methods, Levenberg-Marquardt numerical optimization (from the `lsqnonlin()` function in MATLAB's optimization suite [8]) is used to find n , k_{eq} pairs that minimize the respective error functions.

Method 3 minimizes error in the ordinary $z - \sigma$ domain. No weighting was considered because error and actual measurements are in the same domains. The minimization function is:

$$F = \sum \left[\sigma - k_{eq} z^n \right]^2. \quad (19)$$

Method 4 has an identical error function to that of method 2: both are in the log-log domain and have w_r set to 1. The only difference is that method 4 is numerically

minimized, whereas method 2 is analytically derived. The minimization function is:

$$F = \sum \left[\ln \sigma - \ln k_{eq} - n \ln z \right]^2 . \quad (20)$$

Method 5 is the numerical version of Wong's method, method 1. The minimization function is:

$$F = \sum \sigma^2 \left[\ln \sigma - \ln k_{eq} - n \ln z \right]^2 . \quad (21)$$

Methods 1-5 are summarized in Table 1.

Table 1: Alternative methods to estimate pressure-sinkage parameters.

Method	Type	Domain	Weighting factor, w_r
1. Wong's	Analytical	log-log	σ^2
2. Wong's (modified)	Analytical	log-log	1
3. Least-square-curve-fit	Numerical	$z-\sigma$	N/A
4. Least-square-curve-fit	Numerical	log-log	1
5. Least-square-curve-fit	Numerical	log-log	σ^2

Individual parameter estimation of the 45 pressure-sinkage tests was performed using each of the five methods. The error of a fit for all methods is calculated using Wong's suggestion:

$$\varepsilon = \frac{\sqrt{\frac{\sum (\sigma_m - \sigma_c)^2}{N-2}}}{\frac{\sum \sigma_m}{N}}, \quad (22)$$

where σ_m is measured pressure, σ_c is estimated pressure, and N is the number of data points.

Direct Shear Parameter Estimation

Several soil parameters can be determined using the direct shear test. Specifically, the residual shear stress, τ_{res}, and shear modulus, K, can be determined by fitting the Janosi and Hanamoto equation to each data set, and the cohesion, c, angle of internal friction, φ, can be found using the Mohr-Coulomb failure criteria.

Janosi Hanamoto Equation for Shear Stress

The shear-displacement expression suggested by Janosi and Hanamoto [9] assumed the form of Equation (23) for loose soils:

$$\tau = \tau_{res} \left(1 - e^{\frac{-j}{K}} \right), \quad (23)$$

where τ represents the shear stress and j is the displacement due to shearing. The parameters τ_{res} and K are determined by minimizing the sum of the differences between the experimental value of τ and the estimate at the i^{th} data point in Equation (24) using the Levenberg-Marquardt algorithm:

$$F(K, \tau_{res}) = \sum_{i=1}^{N} \left(\tau_i - \tau_{res} \left(1 - e^{\frac{-j_i}{K}} \right) \right)^2 , \quad (24)$$

The first order KKT optimality condition leads to the following two equations:

$$\frac{\partial F}{\partial K} = 0 \quad (25)$$

$$\frac{\partial F}{\partial \tau_{res}} = 0 \quad (26)$$

where the partial derivatives are determined using a numerical central differences approach.

Mohr-Coulomb Failure Criteria

For a given normal load, the soil is said to fail when it reaches its residual shear stress. According to the Mohr-Coulomb failure criteria [10], a line of best fit can be determined by plotting the residual shear stress, τ_{res}, as a function of normal stress , σ , as follows:

$$\tau_{res} = c + \sigma \tan \varphi, \quad (27)$$

where the intercept is equal to the cohesion and the slope is related to the angle of internal friction. The line of best fit is determined using the closed-form equation for linear fitting over N data points (Equation (28)). The closed-form equation will be useful for propagating the uncertainty later:

$$\begin{bmatrix} \sum_{i=1}^{N}\sigma_i^2 & \sum_{i=1}^{N}\sigma_i \\ \sum_{i=1}^{N}\sigma_i & N \end{bmatrix}\begin{bmatrix} \tan\varphi \\ c \end{bmatrix}=\begin{bmatrix} \sum_{i=1}^{N}\sigma_i\tau_{res,i} \\ \sum_{i=1}^{N}\tau_{res,i} \end{bmatrix}. \quad (28)$$

Wheel Performance Uncertainty Propagation and Verification

This section details the experimental method used to obtain the wheel performance measurements, explains the theory behind the prediction of wheel performance, and describes the derivation behind the method of uncertainty propagation. Since the techniques used in this paper rely on estimates of the stress distribution to determine wheel performance, the ability to measure these quantities allow for a direct comparison of prediction to reality. The uncertainty propagation gives an envelope of system performance that the experimental data can be compared against.

Experimental Methodology

A complete investigation into the performance of the wheel requires insight into several different measures of the wheel-soil interaction. In this paper, physical measurements of contact stresses, force, torque, and sinkage were used to compare to the theoretical model. A single-wheel test rig, shown in Figure 4, was used to empirically investigate the wheel motion under controlled wheel slip and normal loading conditions on the cohesion-less soil [11]. This test rig enables the control of velocities and application of loads through interchangeable running gear within a confined soil bin of dimensions 1.5 m long, 0.7 m wide, and 0.4 m deep. The drawbar pull, wheel torque, and sinkage were measured for a lug-less rigid wheel with a radius of 0.13 m and a width of 0.16 m at slip ratios varying from zero to unity. Tests were run for two different cases: normal loads of 70 N and 135 N.

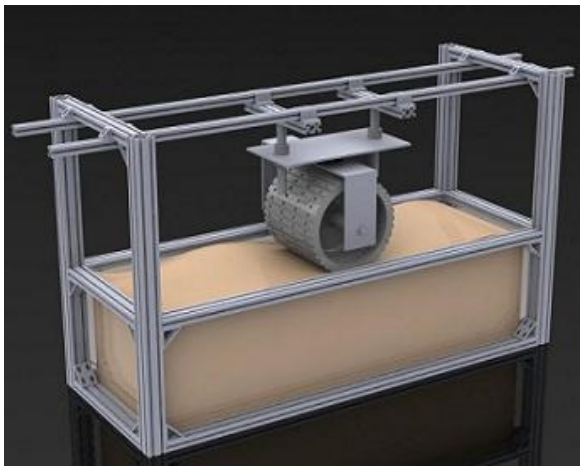

Figure 4: A single wheel test bed was used to measure the drawbar pull, torque, and sinkage at varying slips and normal loads.

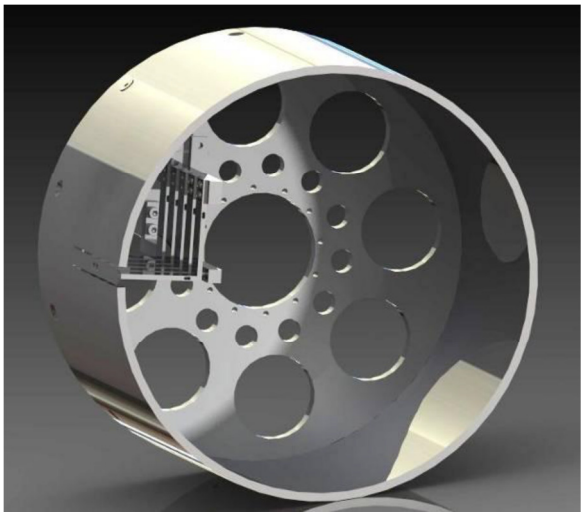

Figure 5: A wheel with a custom force sensor array was used to measure the stress distribution at the contact patch.

To measure the stress distribution at the contact patch of the wheel, an identical wheel with a custom force sensor array located at the wheel surface was used [12]. The force sensors are strain gauge-based flexural elements with interchangeable interface surfaces that are designed for integration with wheels or other running gear. The normal and shear stresses are estimated based on 5 sensors, shown in Figure 6, that are located at discrete points from the center to the edge of the wheel-soil interface.

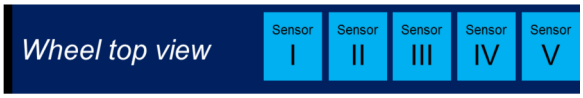

Figure 6: A top view of the wheel shows the layout of the strain gauge-based sensors. Note that the sensors are arranged with Sensor I at the center of the wheel and Sensor V at the outer edge.

Each sensor, shown in Figure 7, is a solid-state L-shaped aluminum flexure instrumented with two full bridge strain gages. The sensor is mounted rigidly to the running gear, and its interface element is exposed to the soil. The interface element is generally subjected to normal, N, and shear, T, loading. These forces cause the flexure elements to deflect in a linear elastic manner. From measured deflection, and given prior calibration data, the applied forces can be uniquely computed, with axial strain intrinsically rejected by the full bridge configuration. Stress can then be inferred assuming uniform pressure distribution over the known sensors' head area.

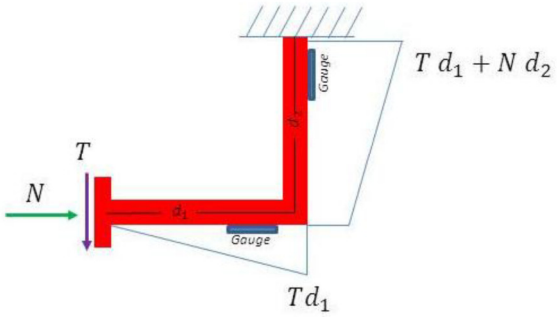

Figure 7: Working scheme of the custom force sensor for interfacial stress measurement.

Mathematical Model of Rigid Wheel on Soft Soil

The rigid wheel free-body diagram based on the work of Wong and Reece [3], shown in Figure 8, is used in this paper to model the interaction between the wheel and the soil. Using this model, the drawbar pull D, torque T, and sinkage z, can be determined for a wheel of weight W, radius r, and wheel width b, travelling at a linear velocity v.

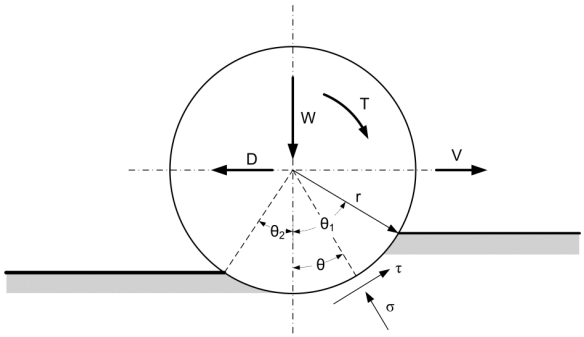

Figure 8: Forces, torque, and stresses on a driven rigid wheel.

The sinkage of the wheel is commonly converted into polar coordinates using the wheel hub as the origin. Once the limits of the contact patch, θ_1 and θ_2, between the wheel and the soil are determined, the drawbar pull and torque can be calculated by integrating the radial and tangential stresses over the wheel.

At a specified slip, i, it is possible to determine the sinkage, forces, and torques that act on a wheel given the soil parameters and wheel properties [3]. A force balance in the vertical direction yields an equation for the weight, W, of the tire:

$$W = rb\int_{-\theta_2}^{\theta_1}\left(\sigma\cos\theta+\tau\sin\theta\right)d\theta, \tag{29}$$

where the normal stress, σ, is determined by Equation (16) and the shear stress, τ, is computed as:

$$\tau = \left(c+\sigma\tan\varphi\right)\left(1-e^{-j/K}\right) \tag{30}$$

where the shear deformation, j, is based on the velocity of the slip:

$$j = r\left[\left(\theta_1-\theta\right)-\left(1-i\right)\left(\sin\theta_1-\sin\theta\right)\right] \tag{31}$$

Based on geometry, the sinkage, z, can be converted to polar coordinates using:

$$z = \left(\cos\theta-\cos\theta_1\right)r \qquad \theta_M \le \theta \le \theta_1 \tag{32}$$

It is important to note that Equation (32) can only be used when the normal stress on the wheel is increasing, which occurs from the front contact angle, θ_1, to a maximum

radial stress, θ_M . At θ_M the stress will begin to decrease in a similar fashion until reaching zero at the rear contact angle, θ_2 . The symmetry between the front and rear regions is employed to derive a relationship for sinkage when the normal stress is decreasing:

$$z = \left(\cos\left(\theta_1 - \left(\frac{\theta - \theta_2}{\theta_M - \theta_2} \right)(\theta_1 - \theta_M) \right) - \cos\theta_1 \right) r \quad -\theta_2 \le \theta \le \theta_M \tag{33}$$

where θ_M can be approximated as a function of θ_1 , i , and two coefficients that give an estimation of the maximum stress, c_1 and c_2 [3]:

$$\theta_M = (c_1 + c_2 i)\theta_1 \tag{34}$$

With the assumption that $\theta_2 = 0$ (which is true when rut recovery is small), the only unknown in Equation (29) becomes θ_1 . The integral in Equation (29) cannot be solved analytically and is solved numerically via an iterative technique. After the front contact angle is determined, the forces (thrust H , motion resistance R , and drawbar pull D) and the input torque, T , can be determined by integrating the stresses over the wheel contact area:

$$H = rb \int_{-\theta_2}^{\theta_1} \tau \cos\theta d\theta \tag{35}$$

$$R = rb \int_{-\theta_2}^{\theta_1} \sigma \sin\theta d\theta \tag{36}$$

$$D = H - R \tag{37}$$

$$T = r^2 b \int_{-\theta_2}^{\theta_1} \tau d\theta \tag{38}$$

Finally, the maximum wheel sinkage, z_0 , can be determined using Equation (32) at $\theta = 0$:

$$z_0 = (1 - \cos\theta_1) r \tag{39}$$

Uncertainty Propagation

The objective of any uncertainty analysis is to obtain an estimate of the overall uncertainty, i.e. uncertainty envelope, of an output given the individual uncertainties of the inputs. Previous work, including Virginia Tech's Center for Vehicle Systems and Safety [13] and the Massachusetts Institute of Technology's Robotic Mobility Group [14], used Polynomial Chaos Theory to quantify the uncertainty associated with terramechanics systems. The method for propagating the uncertainty in this paper is described in [15], and summarized as follows:

Given an arbitrary function, r , that depends on the measured variables $x_1, x_2, \ldots$ whose distributions are normal:

$$r = f(x_1, x_2, \ldots), \tag{40}$$

the variance of r , σ_r^2 , can be determined statistically based on discrete values of the function, r_i , and the mean of the function, r' , using:

$$\sigma_r^2 = \lim_{N \to \infty} \left[\frac{1}{N} \sum_{i=0}^{N} \left(r_i - r' \right)^2 \right]. \tag{41}$$

The difference, δr_i , between a particular value, r_i , and its mean value, r' , can be determined from a Taylor series expansion, where higher order terms are assumed to be negligible:

$$\delta r_i = \left(r_i - r' \right) \cong \left(x_{1i} - x_1' \right) \left(\frac{\partial r}{\partial x_1} \right) + \left(x_{2i} - x_2' \right) \left(\frac{\partial r}{\partial x_2} \right) + \ldots \tag{42}$$

If the equation for δr is substituted into Equation (41), we obtain:

$$\sigma_r^2 \cong \lim_{N \to \infty} \frac{1}{N} \sum_{i=1}^{N} \left[\left(x_{1i} - x_1' \right) \left(\frac{\partial r}{\partial x_1} \right) + \left(x_{2i} - x_2' \right) \left(\frac{\partial r}{\partial x_2} \right) + \ldots \right]^2 \tag{43}$$

which can be rearranged to yield:

$$\sigma_r^2 \cong \lim_{N\to\infty} \frac{1}{N} \sum_{i=1}^{N} \left[\begin{array}{l} \left(x_{1i} - x_1^{'}\right)^2 \left(\frac{\partial r}{\partial x_1}\right)^2 + \left(x_{2i} - x_2^{'}\right)^2 \left(\frac{\partial r}{\partial x_2}\right)^2 \\ +2\left(x_{1i} - x_1^{'}\right)\left(x_{2i} - x_2^{'}\right)\left(\frac{\partial r}{\partial x_1}\right)\left(\frac{\partial r}{\partial x_2}\right) + \ldots \end{array} \right] \tag{44}$$

Note that the variances for x_1 and x_2 can be computed as:

$$\sigma_{x_j}^2 = \lim_{N\to\infty} \left[\frac{1}{N} \sum_{i=1}^{N} \left(x_{ji} - x_j^{'}\right)^2 \right] \tag{45}$$

where Equation (45) can be used to simplify Equation (44), resulting in Equation (46):

$$\sigma_r^2 \cong \sigma_{x_1}^2 \left(\frac{\partial r}{\partial x_1}\right)^2 + \sigma_{x_2}^2 \left(\frac{\partial r}{\partial x_2}\right)^2 + 2\sigma_{x_1 x_2} \left(\frac{\partial r}{\partial x_1}\right)\left(\frac{\partial r}{\partial x_2}\right) + \ldots \tag{46}$$

Note that the covariance term, $\sigma_{x_1 x_2}$, is typically neglected because it is assumed that the variables x_1 and x_2 are statistically independent of one another. The above equation gives the *standard deviation* of the independent variable given the *standard deviation* of the variables that it depends on. A similar statement can be made for the uncertainty, to get the response uncertainty:

$$u_c^2 \cong u_{x_1}^2 \left(\frac{\partial r}{\partial x_1}\right)^2 + u_{x_2}^2 \left(\frac{\partial r}{\partial x_2}\right)^2 + 2u_{x_1 x_2} \left(\frac{\partial r}{\partial x_1}\right)\left(\frac{\partial r}{\partial x_2}\right) + \ldots \tag{47}$$

Equation (47), hence, defines how the uncertainties of underlying variables propagates into the overall response. The specific parameters that contribute to the uncertainty of the wheel performance are listed in Table 5 and Table 6.

RESULTS

Soil Parameter Variability

Pressure-Sinkage Test

A total of 45 pressure-sinkage tests were performed to analyze the bearing characteristics of the soil. The tests were repeated 15 times for three rectangular plates with different widths, b (3, 5, and 7 cm). Parameters were determined using the five different methods outlined previously in previously.

Figure 9 shows the fits produced by the first three methods for a single test. Methods 1 and 3 yield similar curves, though varying slightly. The curve produced by method 2 appears very different and is strongly biased towards fitting the initial data points of each test. Methods 1 and 2 produced results identical to methods 5 and 4, respectively. The same trends of each different method fit are seen in all of the other pressure-sinkage tests.

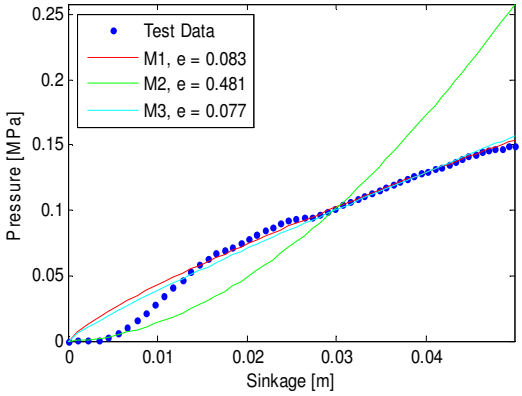

Figure 9: Sample estimation for 5-cm plate.

It is important to recognize that no exponential function will closely fit the actual shape of the data curves. This is a direct consequence of the fact that Bekker's exponential relationship in equation (1) is an empirical estimation, not a physical law, and it does not account well for deviance in the early behavior (when sinkage is less than about 15 mm).

Average values of n, k_{eq}, and least-squares error for each fitting method and plate size are shown in Table 2.

Table 2: Average parameters and error for 3-cm, 5-cm, and 7-cm plates, Bekker's equation.

Plate Width, b (cm)	3			5			7		
Method #	n	$k_{eq,3}$ [MPa/m^n]	error	n	$k_{eq,5}$ [MPa/m^n]	error	n	$k_{eq,7}$ [MPa/m^n]	error
1, 5	1.01	2.48	0.040	0.84	1.90	0.071	1.082	0.231	0.096
2, 4	1.39	9.89	0.196	1.44	25.7	0.276	1.114	0.266	0.220
3	1.03	2.66	0.039	0.89	2.21	0.067	0.976	0.252	0.092

Methods 1, 3 and 5 have relatively small fit errors. The parameters found by methods 2 and 4 are substantially different than those of the other methods; the sinkage exponent n is much higher and the coefficient k_{eq} is much larger. As noted previously, these methods fit low-sinkage data points well but poorly match the rest of the data.

Several important conclusions may be drawn from these results. First, Wong's method (method 1) has proven to be very reliable as compared to a similar numerical method (method 3). Secondly, it gives a very good approximation to the best fit in the $z-\sigma$ domain. Nevertheless, estimation in the log domain and in the $z-\sigma$ domain will yield different parameters. A third observation is that the weighting factor σ^2 is necessary for best results in the log-log domain.

The error found by methods 1 and 3 is comparable. The (n, k_{eq}) parameter pairs found by methods 1 and 3 also produce a similar pressure-sinkage curve, so it is concluded that either method may be used for comparable predictions. It is interesting to note, however, that the individual parameters yielded from methods 1 and 3 can be significantly different despite both yielding a good fit.

Parameter Covariance

The covariance demonstrated by n and k_{eq} requires attention before proceeding to a statistical analysis. Figure 10 illustrates the apparent correlation of Bekker's parameters. Theoretically, every test should yield a similar n, but each plate size should yield a different k_{eq}.

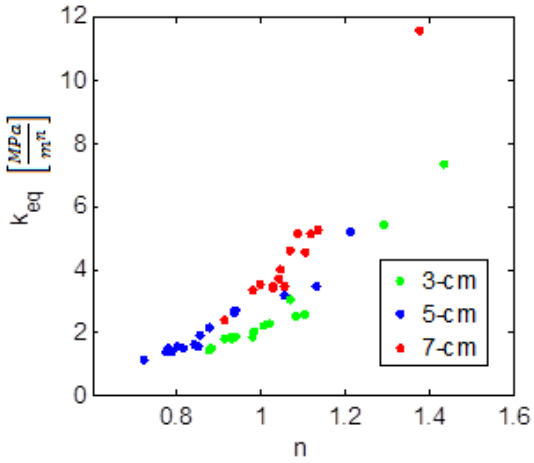

Figure 10: Relationship between n and k_{eq}, Bekker's equation.

In this case, n and k_{eq} show positive correspondence. This correspondence may be explained by noting that modifying the units of k_{eq} has a significant effect. The relationship between n and k_{eq} estimations exist because different combinations may yield a similar pressure prediction, and because the unit of k_{eq} is dependent on n itself:

$$[k\,units] = \frac{[pressure\,units]}{[sinkage\,units]^n} \tag{48}$$

To mitigate this difficulty, Reece's revision of Bekker's equation (Equation (16)) was implemented so that the unit of k_{eq} is always in pressure units and does not depend on n. Applying Equation (16) (instead of Equation (15)) to solve for the parameters resulted in very little *n*-k_{eq}' correlation for our data, as shown in Figure 11. For each plate size, k_{eq}' demonstrated no visible trend with *n*.

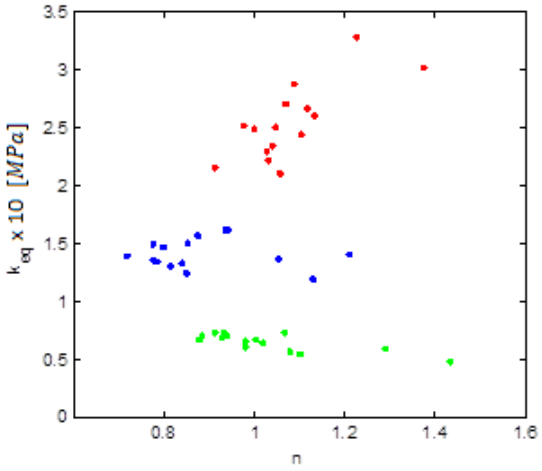

Figure 11: Relationship between n and k_{eq}', Reece's modification.

For each experimental run, Equation (16) was fit to a plot of the pressure as a function of sinkage. The equivalent pressure-sinkage constant, k_{eq}', and exponent of sinkage to plate width, n, found in Reece's equation were determined by minimizing an error function based on the least-squares method (analogous to method 3, described in the parameter estimation section). The mean and standard deviation were calculated to quantify the experimental variability of each soil parameter. The parameters for each data set are recorded in Table 3.

Table 3: Pressure-sinkage parameters and the mean and standard deviation for each plate size, Reece's equation. Values from experimental runs are italicized.

Plate Width, b (cm)	3		5		7	
Test #	n	$k_{eq,3}$' [MPa]	n	$k_{eq,5}$' [MPa]	n	$k_{eq,7}$' [MPa]
1	*0.938*	*0.070*	*1.208*	*0.140*	*1.082*	*0.231*
2	*0.876*	*0.067*	*0.784*	*0.134*	*1.114*	*0.266*
3	*1.289*	*0.059*	*0.774*	*0.149*	*0.976*	*0.252*
4	*1.017*	*0.065*	*0.839*	*0.133*	*0.996*	*0.250*
5	*1.162*	*0.066*	*0.773*	*0.136*	*1.053*	*0.210*
6	*0.928*	*0.068*	*0.983*	*0.160*	*0.960*	*0.217*
7	*0.980*	*0.066*	*0.775*	*0.132*	*1.154*	*0.236*
8	*0.958*	*0.070*	*0.848*	*0.125*	*1.028*	*0.222*
9	*1.434*	*0.048*	*0.716*	*0.139*	*1.066*	*0.270*
10	*0.930*	*0.073*	*1.053*	*0.137*	*1.224*	*0.327*
11	*0.979*	*0.061*	*0.874*	*0.157*	*1.085*	*0.288*
12	*1.002*	*0.067*	*0.938*	*0.162*	*1.102*	*0.245*
13	*0.926*	*0.070*	*1.130*	*0.119*	*1.107*	*0.254*
14	*1.079*	*0.057*	*0.797*	*0.147*	*1.252*	*0.262*
15	*1.061*	*0.057*	*0.851*	*0.851*	*1.440*	*1.440*
Mean	**1.037**	**0.064**	**0.889**	**0.141**	**1.109**	**0.255**
Std. Dev.	**0.152**	**0.007**	**0.145**	**0.013**	**0.123**	**0.032**

The standard deviation of the Reece parameters were propagated to uncertainty in pressure by applying the statistical techniques that resulted in Equation (47). The uncertainty of Reece's model for the pressure, σ, at a given sinkage, z, can be obtained as:

$$u_\sigma^2 \cong u_{k_{eq}^{'}}^2 \left(\frac{\partial \sigma}{\partial k_{eq}^{'}}\right)^2 + u_n^2 \left(\frac{\partial \sigma}{\partial n}\right)^2 \tag{49}$$

where

$$\frac{\partial \sigma}{\partial k_{eq}^{'}} = \left(\frac{z}{b}\right)^n$$
$$\frac{\partial \sigma}{\partial n} = k_{eq}^{'} \left(\frac{z}{b}\right)^n ln\left(\frac{z}{b}\right) \tag{50}$$

and the uncertainties of the independent parameters $u_{k'_{eq}}$ and u_n are made equivalent to the standard deviation of the pressure-sinkage parameters in Table 3.

Figure 12 - Figure 14 show the uncertainty estimation of the pressure-sinkage model for plate widths of 3, 5, and 7 cm, respectively, overlaid with the mean and standard deviation of the experimental pressure data.

As can be seen in Figure 12 - Figure 14, although Reece's model does not precisely capture the pressure-sinkage behavior, the model uncertainty provides a close estimate of the experimental standard deviation.

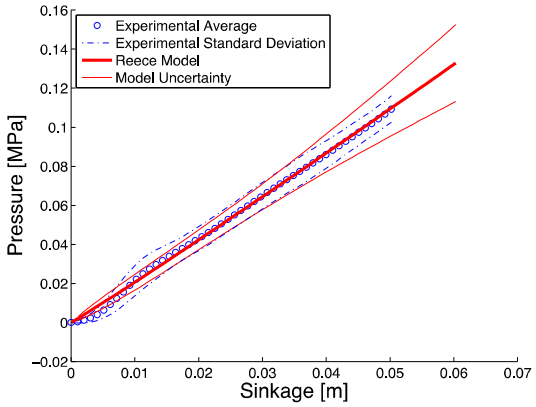

Figure 12: Uncertainty estimation for pressure-sinkage test for 3 cm plate.

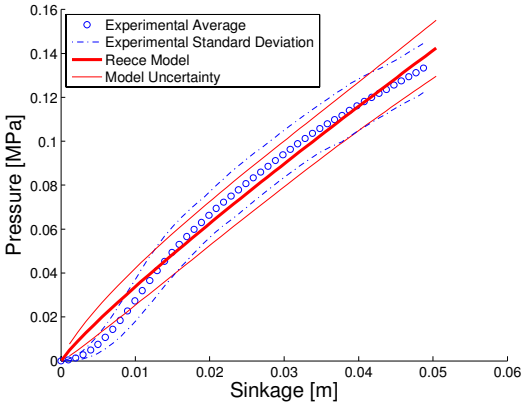

Figure 13: Uncertainty estimation for pressure-sinkage test for 5 cm plate.

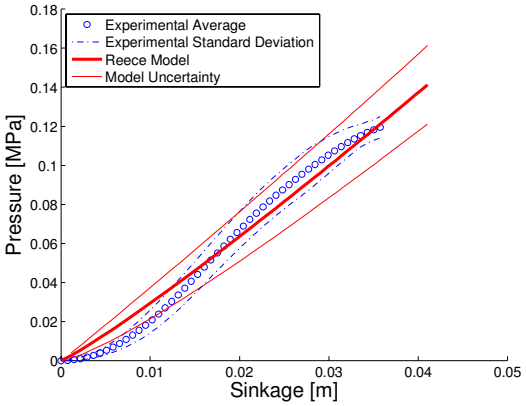

Figure 14: Uncertainty estimation for pressure-sinkage test for 7 cm plate.

In contrast, if the uncertainty were to be determined by the standard deviations of Bekker's parameters, the bounds would be much wider than the experimental deviations, as illustrated in Figure 15 - Figure 17.

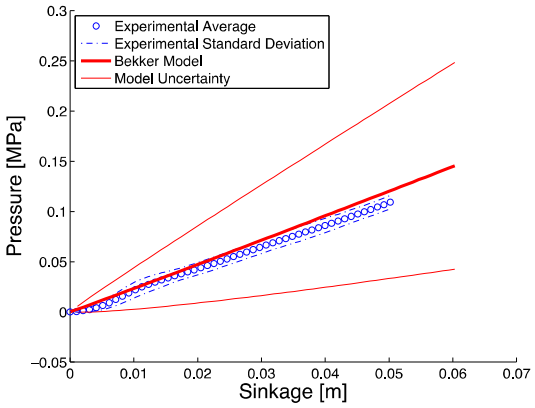

Figure 15: 3 cm plate, Bekker's parameters.

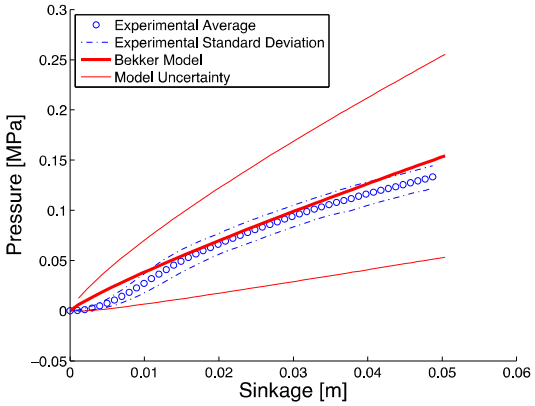

Figure 16: 5 cm plate, Bekker's parameters.

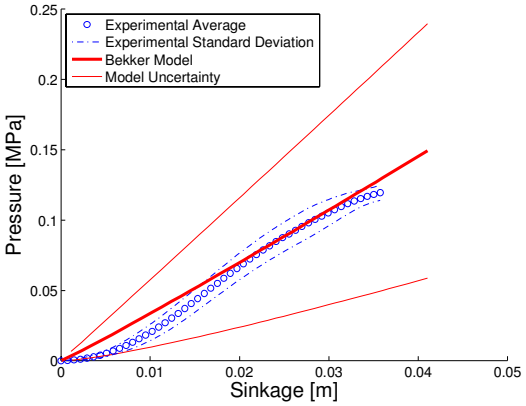

Figure 17: 7 cm plate, Bekker's parameters.

The mean values of Reece's model parameters for the 5 cm plate ($k_{eq,5}' = 0.141$, $n = 0.889$) were used to estimate the mean pressure-sinkage curve for the wheel performance analyses in this study. This plate size was selected because its contact patch area most closely resembles that of the single wheel used in this study.

Direct Shear Test

A total of 12 direct shear tests were performed to analyze the shear characteristics of the dry soil. The tests were repeated three times for four different normal stresses each (2.08, 2.86, 5.33, and 17.83 kPa). For each experimental run that was carried out for the direct shear test, Equation (23) was fit to a plot of the shear stress as a function of shear displacement. The residual shear stress, τ_{res}, and shear modulus, K, found in Equation (23) were determined by minimizing an error function based on the least squares method. The parameters for each data set are recorded in Table 4. The mean and standard deviation are calculated to quantify the variability of each soil parameter.

Table 4: Soil parameters based on shear-displacement curve fits along with the mean and standard deviation for each parameter. Values for experimental runs are italicized.

Normal Stress [kPa]	2.08		2.86		5.33		17.83	
Density [g/cm³]	1.5 (Loose)		1.7 (Dense)		1.7 (Dense)		1.7 (Dense)	
	τ_{max} [Pa]	K [mm]	τ_{max} [Pa]	K [mm]	τ_{max} [Pa]	K [mm]	τ_{max} [Pa]	K [mm]
Test 1	*1363*	*0.498*	*1157*	*0.128*	*1941*	*0.126*	*6423*	*0.145*
Test 2	*1446*	*0.687*	*1797*	*0.130*	*1900*	*0.205*	*6733*	*0.149*
Test 3	*909*	*0.870*	*991*	*0.225*	*2086*	*0.262*	*7042*	*0.117*
Mean	**1239**	**0.685**	**1315**	**0.161**	**1976**	**0.198**	**6733**	**0.137**
Std. Dev.	**289.1**	**0.019**	**425.4**	**0.052**	**97.6**	**0.068**	**309.8**	**0.017**

The results of the analysis in Table 4 were used to determine the cohesion and angle of friction of the soil. The maximum shear stress and applied normal stress are related using Equation (27), and are shown in Figure 18.

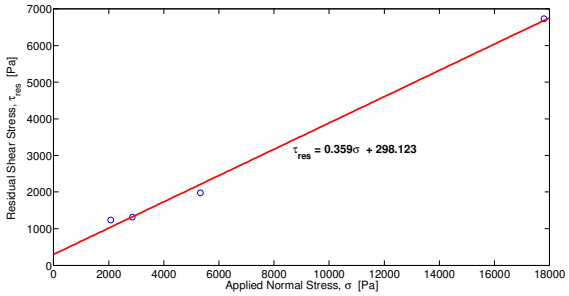

Figure 18: The cohesion and angle of friction of the soil are determined using the Mohr-Coulomb failure criteria. The cohesion is the intercept of the plot and the angle of friction is the slope.

Based on this linear curve fit and Equation (27), the cohesion of the material is equal to 298.123 Pa and the angle of internal friction is equal to 19.735 degrees. Using Equation (47) and Equation (28), the uncertainty is 239.735 Pa and 1.277 degrees for cohesion and internal friction angle, respectively.

To demonstrate the propagation of the variability of the experimental parameters to the uncertainty of Janosi and Hanamoto's model, Equation (47) was applied using the data in Table 4. Figure 19 - Figure 22 compare the uncertainty estimation of the direct shear tests for varying normal stresses to the mean and standard deviation of the experimental data. Although Janosi and Hanamoto's model does not precisely capture the shear-displacement behavior for dense soil, the cohesion and angle of friction

have been shown to be independent of density when using the residual shear stress [10]. It is important to note that the shear modulus is dependent on density. Janosi and Hanamoto's model was used to obtain the mean value of the shear-displacement estimation. The uncertainty of Equation (23) for the shear stress, τ, at a given shear displacement, j, is approximated as:

$$u_\tau^2 \cong u_{\tau_{res}}^2 \left(\frac{\partial \tau}{\partial \tau_{res}} \right)^2 + u_K^2 \left(\frac{\partial \tau}{\partial K} \right)^2 \tag{51}$$

where

$$\begin{aligned} \frac{\partial \tau}{\partial \tau_{res}} &= 1 - e^{-j/K} \\ \frac{\partial \tau}{\partial K} &= \tau_{res} e^{-j/K} \left(\frac{-j}{K^2} \right), \end{aligned} \tag{52}$$

and the uncertainties, $u_{\tau_{res}}$ and u_K, of the independent parameters are determined by the standard deviation of the parameters determined by the direct shear tests in Table 4.

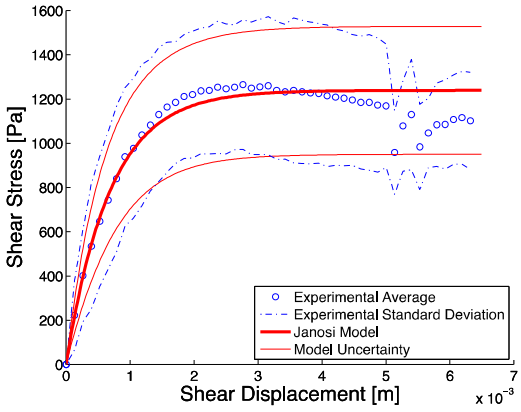

Figure 19: Model uncertainty estimation and experimental standard deviation for a normal stress of 2.08 kPa on loose soil.

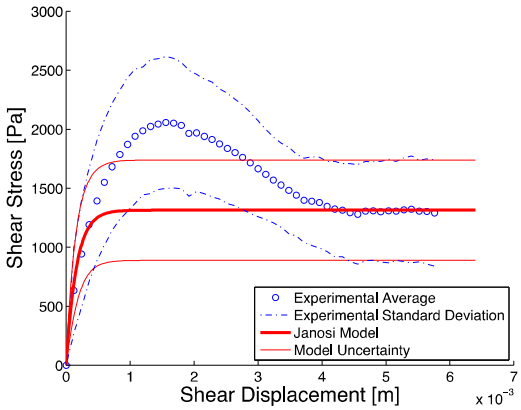

Figure 20: Model uncertainty estimation and experimental standard deviation for a normal stress of 2.86 kPa on dense soil.

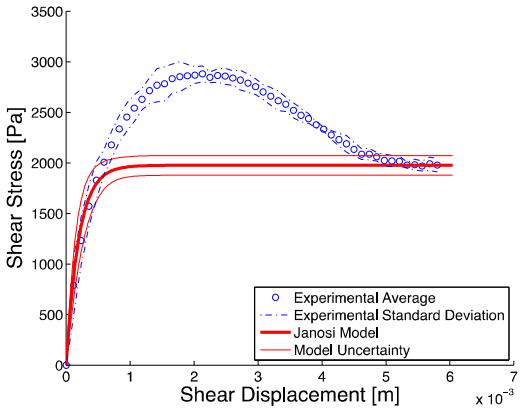

Figure 21: Model uncertainty estimation and experimental standard deviation for a normal stress of 5.33 kPa on dense soil.

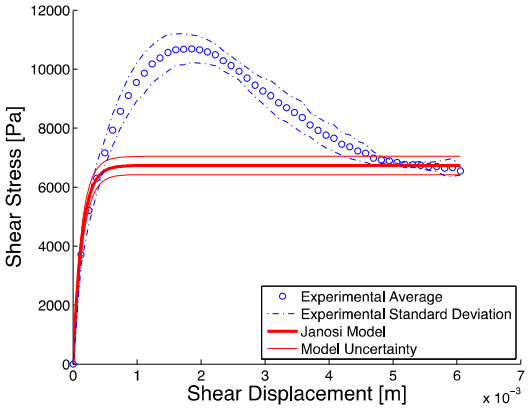

Figure 22: Model uncertainty estimation and experimental standard deviation for a normal stress of 17.83 kPa on dense soil.

Wheel Performance Uncertainty

Force sensors at five locations across the width of the wheel (Figure 6) measured the normal and tangential stress distributions (Figure 23 - Figure 28). Similarly, the drawbar pull, torque, and wheel sinkage at five different slip ratios ranging from -70% to 70%, and two different normal loads of 70 N and 135 N, shown in Figure 29 - Figure 34, were measured using the single-wheel test bed in Figure 4.

The uncertainty estimation method is used along with the soil parameters in Table 5 and wheel properties in Table 6 to compare the wheel performance model to the experimental values of wheel performance. The normal and tangential stresses at the wheel-soil interface were calculated from Equations (16) and (30), respectively, and plotted in Figure 23 - Figure 28. The drawbar pull, torque, and wheel sinkage at three different slip ratios ranging from 10% to 70%, and two different normal loads of 70 N and 135 N, shown in Figure 29 - Figure 34, were calculated using Equations (37), (38), and (39).

Table 5: Soil parameters.

Parameter	Value	Uncertainty	Units
Pressure-sinkage constant, $k'_{eq,b=5cm}$	1.41×10^5	1.30×10^4	Pa
Exponent of (sinkage\width), $n_{b=5cm}$	0.889	0.145	-
Cohesion, c	298.123	239.735	Pa
Angle of internal friction, φ	19.735	1.277	degrees
Shear modulus, K	6.851×10^{-4}	1.858×10^{-4}	m
Coefficient for maximum stress, c_1	0.5	0.2	-
Coefficient for maximum stress, c_2	0.5	0.2	-

Table 6: Wheel properties.

Parameter	Value	Uncertainty	Units
Normal force, F_z	70, 135	5%	N
Wheel radius, r	0.13	0	m
Wheel width, b	0.16	0	m

The model uncertainties of the normal and tangential stresses are plotted against the experimental data in Figure 23 - Figure 28. The uncertainty bars are determined numerically [16] using a finite differencing technique to obtain the sensitivity of the wheel performance with respect to each variable. Note that the model uncertainty envelope does not sufficiently capture the experimental data.

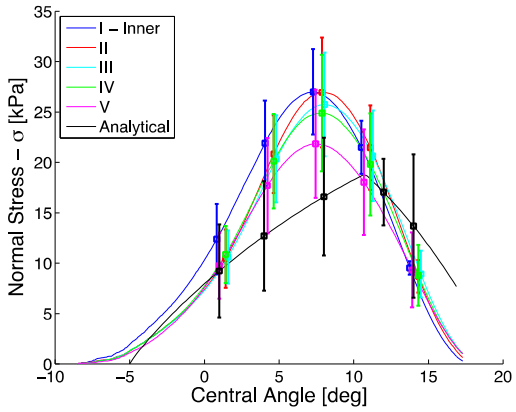

Figure 23: Normal stress vs. contact angle for 10% slip.

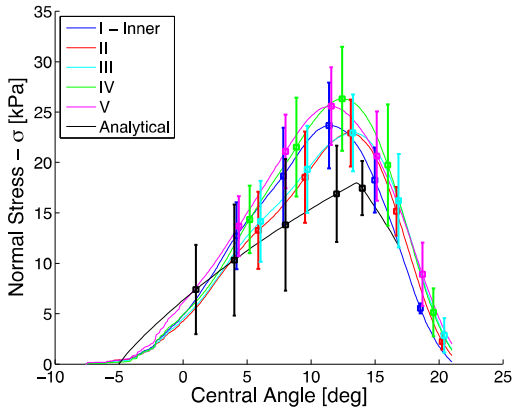

Figure 24: Normal stress vs. contact angle for 30% slip.

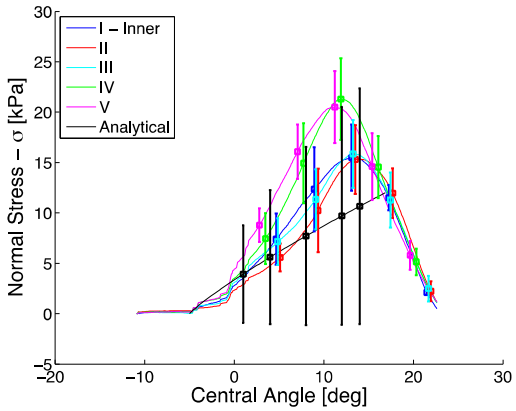

Figure 25: Normal stress vs. contact angle for 70% slip.

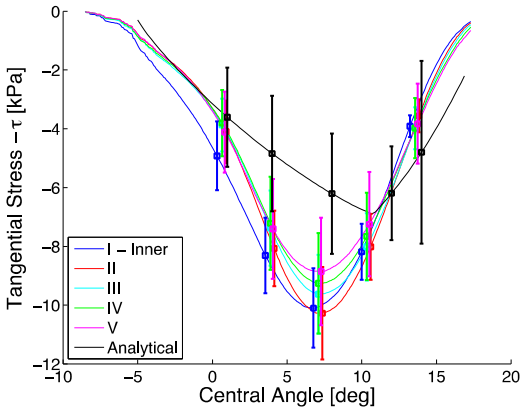

Figure 26: Tangential stress vs. contact angle for 10% slip.

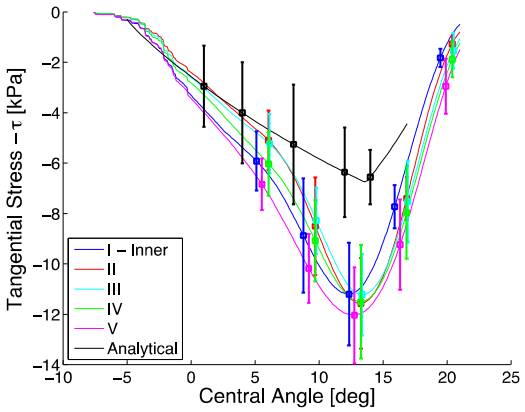

Figure 27: Tangential stress vs. contact angle for 30% slip.

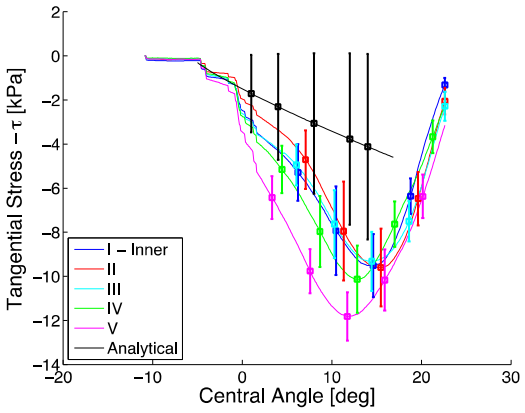

Figure 28: Tangential stress vs. contact angle for 70% slip.

Finally, the uncertainty of the soil parameters is propagated to the drawbar pull, torque, and sinkage of the wheel, as shown in Figure 29 - Figure 34. The uncertainty bars are determined numerically [16] using a finite differencing technique to obtain the sensitivity of the wheel performance with respect to each variable and are plotted along with the measurements based off the individual experimental runs. Note that the model uncertainty envelope does not sufficiently capture the experimental data, particularly in torque and sinkage.

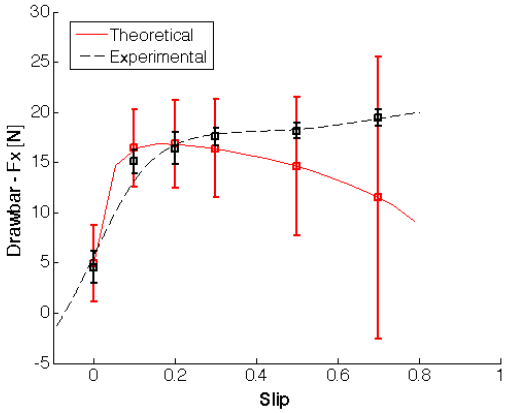

Figure 29: The uncertainty of the drawbar pull of the wheel for a plate size of 5 cm x 16 cm and vertical force of 70N.

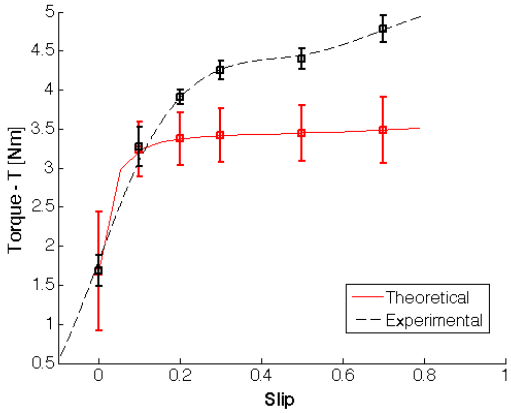

Figure 30: The uncertainty of the torque of the wheel for a plate size of 5 cm x 16 cm and vertical force of 70N.

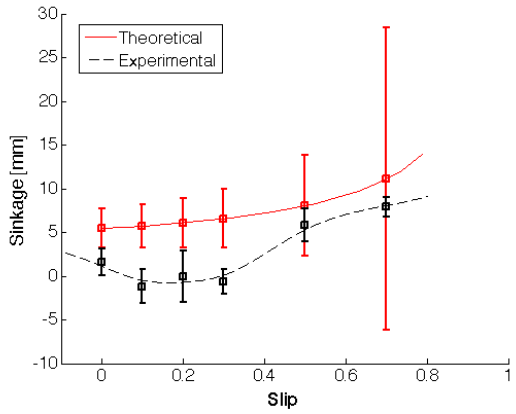

Figure 31: The uncertainty of the sinkage of the wheel for a plate size of 5 cm x 16 cm and vertical force of 70N.

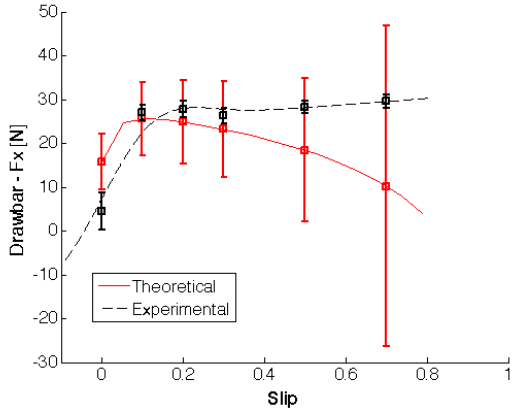

Figure 32: The uncertainty of the drawbar pull of the wheel for a plate size of 5 cm x 16 cm and vertical force of 135N.

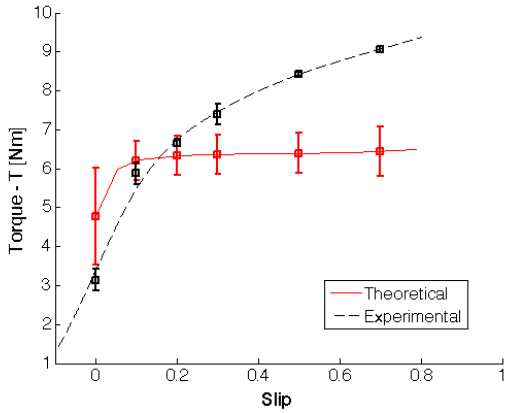

Figure 33: The uncertainty of the torque of the wheel for a plate size of 5 cm x 16 cm and vertical force of 135N.

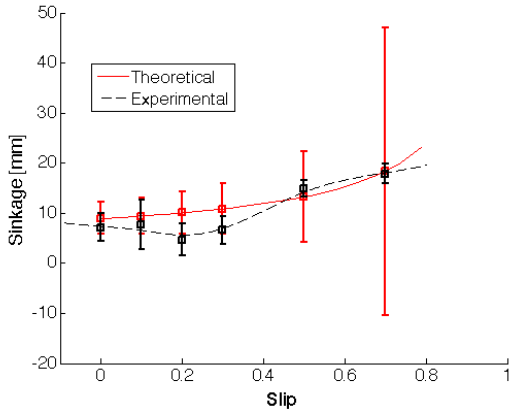

Figure 34: The uncertainty of the sinkage of the wheel for a plate size of 5 cm x 16 cm and vertical force of 135N.

SUMMARY

Soil Parameter Variability

The first objective of this paper was to characterize the variability of measured soil parameters given experimental data. To determine the soil parameters associated with normal loads, the pressure and sinkage were measured with a plate that penetrated the soil under controlled test conditions. To determine the soil parameters associated with shearing loads, a standard direct shear test was performed under various normal loads. The individual soil parameters were obtained from the pressure-sinkage tests by fitting the dimensionless form of Reece's equation to each experimental data set. Similarly, Janosi and Hanamoto's equation for shearing was fit to the direct shear test to determine the soil parameters for each experimental data set. The mean and standard deviation were calculated to quantify the variability of each soil parameter. This experimental variability was used to calculate the uncertainty of the soil stress. Based on Figure 12 - Figure 14 and Figure 19 - Figure 22, the model uncertainties show good agreement with the actual standard deviations of the experimental measurements. Since the model parameters were estimated from the same experimental data, this uncertainty correlation validates the uncertainty propagation theory employed in this paper.

Wheel Performance Uncertainty

The second objective of this contribution was to quantify the uncertainty in wheel performance. Such an investigation requires that the wheel can be accurately modeled. The sinkage of the rigid wheel model, based on the work of Wong and Reece, was determined by relating

the weight of the wheel and the stresses acting on it in the vertical direction. Given the uncertainties of the individual soil parameters, it was possible to determine the overall uncertainty of the wheel performance (drawbar pull, torque, and sinkage) using the statistical techniques described in the uncertainty propagation section. The uncertainties of the normal and tangential stresses were plotted against the experimental data for a single wheel traversing over the soil in Figure 23 - Figure 28. Additionally, the uncertainty of the soil parameters was propagated to the drawbar pull, torque, and sinkage of the wheel, as shown in Figure 29 - Figure 34. The wheel performance model fails to capture much of the experimental stress data and has little overlap with the drawbar pull, torque, and sinkage. It is evident from the results that the classical terramechanics model used in this paper is not suitable for the analysis of lightweight vehicles that exhibit relatively low ground pressures (i.e. 15-35 kPa).

Several modifications could be made improve the accuracy of this model for lightweight vehicles. For example, the flat plate assumption of pressure-sinkage models has been shown to be inaccurate for lightweight vehicles and would likely benefit from revisions according to the recent results for diameter-dependent models reported in [17]. Further, the shear characteristics of the soil, shown in Figure 19 - Figure 22, are not adequately captured and could be more accurately estimated from making a modification to Equation (23) such as in [18] to account for the nonlinear “hump” that occurs in dense soil. Lastly, based on the size of the vehicle and the nature of the terrain, alternate methods could be employed to capture the behavior of each individual soil particle [19].

REFERENCES

[1] M. G. Bekker, *Off-the-road locomotion; research and development in terramechanics*. Ann Arbor,: University of Michigan Press, 1960.

[2] L. W. Beegle, G. H. Peters, G. S. Mungas, G. H. Bearman, J. A. Smith, and R. C. Anderson, "Mojave Martian Simulant: A New Martian Soil Simulant," *Lunar and Planetary Science XXXVIII,* 2007.

[3] J. Y. Wong and A. Reece, "Prediction of rigid wheel performance based on the analysis of soil-wheel stresses part I. Performance of driven rigid wheels," *Journal of Terramechanics,* vol. 4, pp. 81-98, 1967.

[4] E. Micklethwait and G. Britain, *Soil mechanics in relation to fighting vehicles*, 1944.

[5] J. Y. Wong, *Terramechanics and off-road vehicle engineering terrain behaviour, off-road vehicle performance and design*, 2nd ed ed. Amsterdam: Elsevier, 2010.

[6] K. Terzaghi, R. B. Peck, and G. Mesri, *Soil mechanics in engineering practice*: Wiley-Interscience, 1996.

[7] J. Y. Wong, "Data-Processing Methodology in the Characterization of the Mechanical-Properties of Terrain," *Journal of Terramechanics,* vol. 17, pp. 13-41, 1980.

[8] T. F. Coleman, M. A. Branch, and A. Grace, *Optimization toolbox*: MathWorks, 1999.

[9] Z. Janosi and B. Hanamoto, "The analytical determination of drawbar pull as a function of slip for tracked vehicles in deformable soils," in *Proc of the 1st Int Conf Mech Soil–Vehicle Systems. Turin, Italy*, 1961.

[10] C. Senatore and K. D. Iagnemma, "Direct shear behaviour of dry, granular soils for low normal stress with application to lightweight robotic vehicle modelling," in *17th International Conference on Terrain-Vehicle Systems ISTVS, Blacksburg, Virginia, USA*, ed, 2011.

[11] K. Iagnemma, *A Laboratory Single Wheel Testbed for Studying Planetary Rover Wheel-Terrain Interaction*. Massachusetts Institute of Technology, Cambridge, MA, 2005.

[12] C. Senatore, M. Wulfmeier, P. Jayakumar, J. Maclennan, and K. Iagnemma, "Investigation of Stress and Failure in Granular Soils For Lightweight Robotic Vehicle Applications," in *Proceedings of the Ground Vehicle Systems Engineering and Technology Symposium*, Michigan, 2012.

[13] L. Li and C. Sandu, "On the impact of cargo weight, vehicle parameters, and terrain characteristics on the prediction of traction for off-road vehicles," *Journal of Terramechanics,* vol. 44, pp. 221-238, 2007.

[14] G. Kewlani, J. Crawford, and K. Iagnemma, "A polynomial chaos approach to the analysis of vehicle dynamics under uncertainty," *Vehicle System Dynamics,* vol. 50, pp. 749-774, 2012.

[15] B. N. Taylor and C. E. Kuyatt, "NIST Technical Note 1297," *Guidelines for evaluating and expressing the uncertainty of NIST measurement results,* 1994.

[16] S. A. Klein and F. L. Alvarado, "Engineering equation solver," *F-Chart Software,* 2002.

[17] G. Meirion-Griffith and M. Spenko, "A modified pressure–sinkage model for small, rigid wheels on deformable terrains," *Journal of Terramechanics,* vol. 48, pp. 149-155, 2011.

[18] C. Senatore and K. D. Iagnemma, "Direct shear behaviour of dry, granular soils for low normal stress with application to lightweight robotic vehicle modelling," *Proceedings of the International*

Symposium of the International Society of Terrain-Vehicle Systems, 2011.

[19] D. Negrut, H. Mazhar, D. Melanz, D. Lamb, P. Jayakumar, M. Letherwood*, et al.*, "Investigating the Mobility of Light Autonomous Tracked Vehicles using a High Performance Computing Simulation Capability," in *Proceedings of the Ground Vehicle Systems Engineering and Technology Symposium*, Michigan, 2012.